








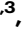



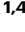





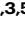
Parity-dependent state transfer for direct entanglement generation

Received: 3 July 2024

Accepted: 3 March 2025

Published online: 18 March 2025

 Check for updates

F. A. Roy ^{1,2,6} ✉, J. H. Romeiro ^{1,3,6} ✉, L. Koch ^{1,3}, I. Tsitsilin^{1,3}, J. Schirk^{1,3}, N. J. Glaser ^{1,3}, N. Bruckmoser ^{1,3}, M. Singh^{1,3}, F. X. Haslbeck ^{1,3}, G. B. P. Huber ^{1,3}, G. Krylov ^{1,3}, A. Marx ¹, F. Pfeiffer ^{1,3}, C. M. F. Schneider ^{1,3}, C. Schweizer ^{1,4}, F. Wallner ^{1,3}, D. Bunch ^{1,3}, L. Richard^{1,3}, L. Södergren ^{1,3}, K. Liegener ^{1,3}, M. Werninghaus ^{1,3} & S. Filipp ^{1,3,5}

As quantum information technologies advance, challenges in scaling and connectivity persist, particularly the need for long-range qubit connectivity and efficient entanglement generation. Perfect State Transfer enables time-optimal state transfer between distant qubits using only nearest-neighbor couplings, enhancing device connectivity. Moreover, the transfer protocol results in effective parity-dependent non-local interactions, extending its utility to entanglement generation. Here, we experimentally demonstrate Perfect State Transfer and multi-qubit entanglement generation on a chain of six superconducting transmon qubits with tunable couplers, controlled via parametric drives. By simultaneously activating and engineering all couplings, we implement the transfer for up to six qubits, verifying single-excitation dynamics for different initial states. Extending the protocol to multiple excitations, we confirm its parity-dependent nature, where excitation number controls the phase of the transferred state. Finally, leveraging this property, we prepare a Greenberger-Horne-Zeilinger state using a single transfer operation, showcasing potential of Perfect State Transfer for efficient entanglement generation.

Quantum information technologies have evolved significantly in the past 20 years and are now at the verge of demonstrating useful applications of quantum computing^{1–5}. Nonetheless, many technologies are facing limitations in the scalability of their platform. In particular, efficiently connecting distant qubits within the same processing unit, and even between different processing units, poses a significant challenge for the generation of highly entangled states. Qubit shuttling has proven to be a successful solution to the problem of connectivity for several different platforms^{6–11}. Nevertheless, some platforms feature qubits that are static in nature, as is the case for solid-state

technologies such as superconducting qubits, making this scheme impossible to use. In this scenario, information has to be moved via a series of swap operations between adjacent qubits until it reaches its destination. As a result, entanglement generation is generally limited and requires sequences of two-qubit and single-qubit gates to achieve the desired state. Alternatively, there have been proposals and demonstrations having multiple qubits coupled to a common element to increase connectivity and to generate many-body entanglement. These protocols are either designed for a limited number of qubits embedded in low-connectivity architectures^{12–16}, or require specially

¹Walther-Meißner-Institut, Bayerische Akademie der Wissenschaften, Garching, Germany. ²Theoretical Physics, Saarland University, Saarbrücken, Germany. ³Department of Physics, Technical University of Munich, TUM School of Natural Sciences, Garching, Germany. ⁴Fakultät für Physik, Ludwig-Maximilians-Universität München, München, Germany. ⁵Munich Center for Quantum Science and Technology (MCQST), München, Germany. ⁶These authors contributed equally: F. A. Roy, J. H. Romeiro. ✉e-mail: federico.roy@wmi.badw.de; joao.romeiro@wmi.badw.de

designed architectures where all qubits involved must share a common coupling element^{17–21}. Consequently, both approaches face limitations in further scaling up many-body entanglement and in coupling genuinely distant qubits.

In this context, Perfect State Transfer (PST) provides an alternative approach to efficiently couple and entangle multiple qubits. In PST, an arbitrary number of qubits is assumed to be coupled along a linear chain with no extra elements, making it a more viable technique for scalable architectures. By activating all couplings in the chain and controlling the strength of the time-independent couplings, quantum states are time-optimally transferred between the qubits on either end of the chain^{22–35}. The same configuration of coupling strengths also result in state transfers between all pairs of mirror-symmetric qubits, i.e. equidistant from the center of the chain. In fact, when considering multiple excitations, the phase of the transferred state will depend on the parity of excitations present between the initial and final transfer locations, as described in detail in³⁶. This gives rise to multi-qubit interaction terms that can be utilised for efficient many-body entanglement creation, as well as for implementing multi-qubit gates^{36–39}. Compared to previous approaches, PST yields non-local connectivity between qubits and provides a method to efficiently generate entanglement without the need for modifications to the hardware. However, experimental work so far has been limited to transfers with excitations only present in the ends of the chain^{40–52}.

Here, we experimentally demonstrate the properties of PST in the presence of multiple excitations throughout the chain. Using superconducting transmon qubits⁵³ and parametrically driven tunable couplers⁵⁴, we implement and control the required couplings and perform the operation for different lengths of chains and prepared initial states. Our results show that excitations transfer from each initial qubit to its mirror-symmetric counterpart. By transferring a superposition state, we directly observe the dependence of the final phase to the number parity of excitations, as predicted by theory. Harnessing these properties, we generate a three-qubit Greenberger-Horne-Zeilinger (GHZ) state with a single PST operation. Finally, using the theory of graph states, we show how this method can be

generalised to larger qubit numbers, showcasing the usefulness of the PST protocol for scalable quantum hardware.

Results

Device description

Experiments are carried out on a superconducting device hosting six fixed-frequency transmon qubits, (q_i), each coupled in a ring layout to their two nearest neighbours via tunable couplers, (c_j), shown in Fig. 1a. All qubits have individual drive lines and readout resonators for single-qubit control and measurement, respectively. The Hamiltonian of this system is given by

$$\begin{aligned} \hat{H}/\hbar = & \sum_{1 \leq i \leq 6} \omega_{q_i} \hat{a}_{q_i}^\dagger \hat{a}_{q_i} + \frac{\alpha_{q_i}}{2} \hat{a}_{q_i}^\dagger \hat{a}_{q_i}^\dagger \hat{a}_{q_i} \hat{a}_{q_i} \\ & + \sum_{1 \leq j \leq 6} \omega_{c_j} (\phi_{c_j}) \hat{a}_{c_j}^\dagger \hat{a}_{c_j} + \frac{\alpha_{c_j}}{2} \hat{a}_{c_j}^\dagger \hat{a}_{c_j}^\dagger \hat{a}_{c_j} \hat{a}_{c_j} \\ & + \sum_{\langle i,j \rangle} \frac{g_{ij}}{2} (\hat{a}_{q_i}^\dagger - \hat{a}_{q_i}) (\hat{a}_{c_j}^\dagger - \hat{a}_{c_j}), \end{aligned} \quad (1)$$

where a and a^\dagger are the creation and annihilation operators for qubits (q_i) and couplers (c_j), with frequencies and anharmonicities given by ω_{q_i/c_j} and α_{q_i/c_j} , respectively. The strength of static couplings between qubits and their neighbouring couplers is given by g_{ij} . The coupler frequencies can be individually tuned by applying external magnetic fields ϕ_{c_j} . Qubit populations are measured through dispersive readout. Measurement errors are characterised using an assignment matrix and mitigated by applying matrix inversion⁵⁵. A circuit diagram representing all qubits and couplers in the device is shown in Fig. 1b and device parameters are given in Supplementary Table 1.

Local qubit-qubit interactions are activated via parametric drives on the respective tunable couplers. By applying the external flux $\phi_{c_j}(t) = \phi_{dc} + A_j \cos(\Delta_j t/k)$, we modulate the coupler at the k -th harmonic of the difference frequency Δ_j between adjacent qubits, generating an effective interaction between them⁵⁴, as shown in Fig. 1c.

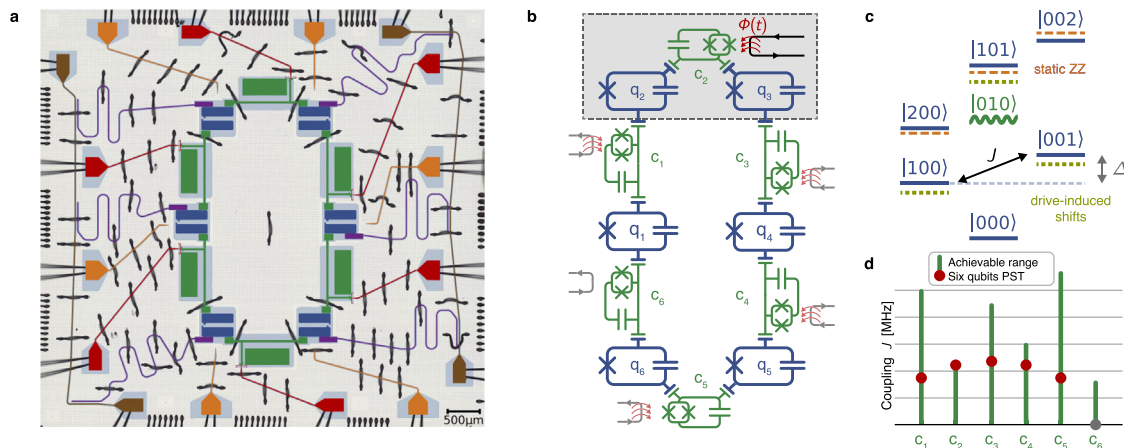


Fig. 1 | Device and parametric coupling. **a** False-colour image of the six-qubits device. Fixed-frequency transmon qubits (blue) are arranged in a ring with tunable transmon couplers (green) between them to mediate couplings. Individual coupler flux lines (red) and qubit drive lines (orange) enable full control of the system. Individual readout resonators (purple) coupled to feed lines (brown) on either side of the chip are used to readout the qubits. Wire bonds (black) connect all ground planes and the PCB lines to lines on the chip. **b** Circuit diagram representing the device. All qubits (blue) couple capacitively to the couplers (green) on either side. The couplers are tuned in frequency via the flux $\phi(t)$ (red) threading through their respective SQUID loop. Parametric drives are used to activate and control effective couplings between qubits. **c** Schematic energy level diagram of two neighbouring

qubits (blue) and the coupler (green). The states are labelled as $|q\ c\ q\rangle$. A parametric flux drive modulates the coupler at the difference frequency of the qubits Δ (grey arrow) activating the effective coupling J (black arrow). Yellow dashed lines represent the shifted levels induced by the drive. ZZ shifts due to the interaction of levels with two excitations are shown in orange. **d** Effective coupling strengths between all neighbouring qubit pairs on the device. Green lines indicate the full range of coupling strength achievable by varying the amplitude of the parametric drive of each coupler. Red dots show the choice of coupling following the PST solution for $N=6$. Coupler c_6 is not modulated (grey dot), turning off the interaction on this edge of the ring.

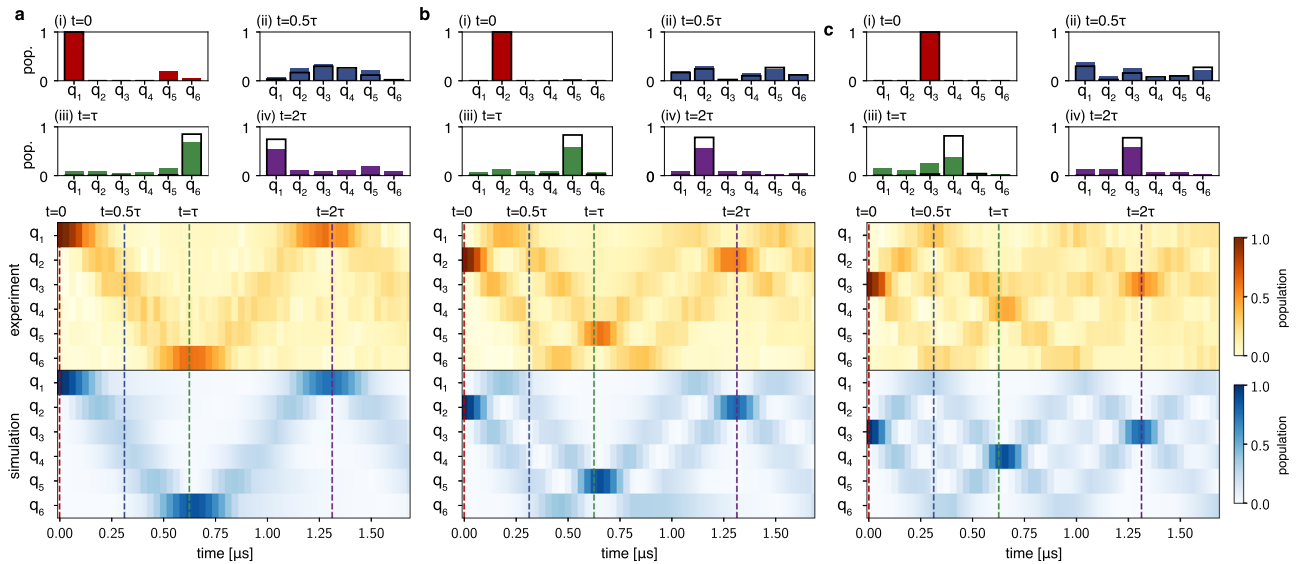


Fig. 2 | Perfect state transfer protocol. Single-excitation dynamics are shown for excitations starting on an outer (a), intermediate (b) and centre (c) qubit for a chain of six qubits. Experimentally measured populations are visualised in a contour plot (middle) and compared to simulations (bottom), which include the effect of relaxation on the qubits. The solid-bar plots (i–iv) show the measured population in all qubits at times $t = 0, 0.5\tau, \tau, 2\tau$ for $\tau = 640$ ns. Black wireframes indicate the expected populations from simulation.

Since the couplers are in the dispersive regime ($|\omega_{c_j} - \omega_{q_i}| \gg g_{ij}$) they can be decoupled from the qubit dynamics by performing a time-dependent Schrieffer-Wolff transformation⁵⁶. Then, truncating the qubit states to the computational subspace yields the effective system Hamiltonian

$$\hat{H}_{\text{eff}}/\hbar = \sum_{1 \leq i \leq 6} \left[J_i (\hat{\sigma}_i^- \hat{\sigma}_{i'}^+ + \text{h.c.}) + \frac{\zeta_i}{4} (\mathbb{1}_i \mathbb{1}_{i'} - \mathbb{1}_i \sigma_i^z - \sigma_i^z \mathbb{1}_{i'} + \sigma_i^z \sigma_{i'}^z) \right]. \quad (2)$$

Here, σ^\pm are the raising and lowering operators, σ^z denotes the Pauli Z operator, $\mathbb{1}$ denotes the identity and $i' \equiv (i \bmod 6) + 1$ indicates the index which succeeds i . Due to the anharmonicity of the transmon, hybridisation between states with two excitations results in unwanted ZZ interactions^{57,58}, whose strength ζ_i depends on the biasing ϕ_{dc} of the couplers. The effective coupling strengths J_i from modulating the k -th harmonic between adjacent qubits i and i' can be tuned by changing the amplitude A_i^k of the respective parametric drive, resulting in

$$J_i \approx \frac{\partial^k \omega_{c_i}}{\partial \phi^k} \Big|_{\phi_{\text{dc}}} \frac{g_{ii'} g_{i'i} A_i^k}{\Delta_i^2 2}. \quad (3)$$

The ranges of achievable experimental couplings for our devices, shown in Fig. 1d, are limited by the onset of higher-order error processes at large modulation amplitudes⁶⁰. Without parametric drive, the effective couplings between adjacent qubits are largely suppressed, with ratios $g/\Delta < 0.02$ for all pairs, except for qubits q_3 and q_4 which partially hybridise ($g/\Delta = 0.16$) due to their small frequency difference. Therefore, utilising parametric drives enables us to control the active couplings on the device and their relative strengths.

Perfect state transfer protocol

In a chain of N coupled qubits

$$\hat{H}_{\text{chain}}/\hbar = \sum_{n=1}^{N-1} J_n (\hat{\sigma}_n^- \hat{\sigma}_{n+1}^+ + \text{h.c.}), \quad (4)$$

a PST is realised by setting the coupling strengths as

$$J_n = \frac{\pi}{2\tau} \sqrt{n(N-n)}, \quad (5)$$

resulting in a state transfer from any qubit and its mirror-symmetric qubit in the transfer time τ . Notably, PST provides the time-optimal solution to transfer states between the ends of the chain^{61,62}.

We implement PST on a chain of $N = 6$ qubits with a transfer time of $\tau = 640$ ns by setting the coupling strengths according to the PST formula in Eq. (5), as shown in Fig. 1d. The coupling strengths are initially calibrated by individually driving each coupler and sweeping the respective drive amplitude. Then, all drives are applied simultaneously and their frequencies and amplitudes are further optimised using a closed-loop routine^{63,64} to compensate for shifts caused by neighbouring drives (see Methods).

We vary the duration of the applied drives and observe transfer dynamics for different initial locations by measuring the excited state population on all qubits. When the excitation is prepared on one of the outer qubits of the chain, it spreads out to the neighbouring qubits forming a single wave-packet structure, as shown in Fig. 2a when qubit q_1 is initially excited. At the transfer time $\tau = 640$ ns, the excitation refocuses on qubit q_6 , located at the other end of the chain. The process repeats every integer multiple of the transfer time, with the excitation alternating between the two ends of the chain. Relevant stages of the transfer dynamics are highlighted in subplots (i–iv). If instead the excitation is prepared on one of the intermediate qubits, as shown in Fig. 2b for q_2 , the excitation first spreads out in two separate wave-packets travelling in opposite directions. Both components then eventually reflect off the closed boundaries and refocus at the mirror-symmetric qubit, q_5 , after the transfer time τ . The process repeats itself until decoherence effects of the qubits become dominant. Finally, when preparing the excitation on one of the centre qubits, as shown in Fig. 2c for q_3 , the dynamics exhibit multiple splittings, yet the excitation refocuses at integer multiples of τ , as in the other cases.

We simulate the perfect dynamics of PST by evolving the chain Hamiltonian in Eq. (4) in the single-excitation manifold with the ideal coupling strengths J_n from Eq. (5). Relaxation effects are included with the addition of non-Hermitian diagonal terms $-i\pi\hbar\Gamma_1^n$, where $\Gamma_1^n = 1/T_1^n$

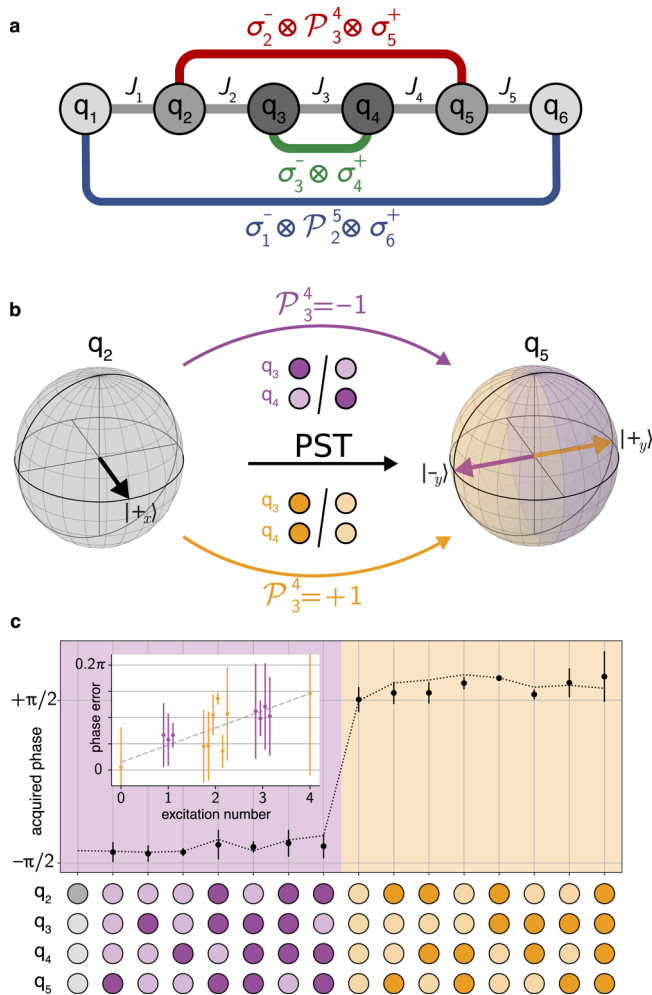


Fig. 3 | Parity-dependence of the PST protocol with multiple excitations on a six-qubit chain. **a** Schematic of the qubit chain with effective PST couplings. Qubits (circles) are connected in a chain by nearest neighbour couplings (grey lines). The effective multi-qubit interactions contain hopping terms $\sigma^- \sigma^+$ between the outer (blue), intermediate (red) and centre qubits (green), and include additionally the parity operator applied to all qubits in between. **b** A superposition state $|+\rangle_x$ prepared on qubit q_2 (left) acquires a phase of $\pm \pi/2$ when transferred to q_5 (right). The sign of the phase is controlled by the number parity \hat{P}_3^4 of the excitations on qubits q_3 and q_4 (centre). **c** Acquired phase in the transfer from qubit q_1 to q_6 for all configurations of the inner qubits q_2, q_3, q_4 and q_5 . The phase is given by the x - y angle of the state of q_6 after the transfer, as measured by quantum state tomography. Values and error bars (standard deviation) are obtained from the phases measured from four different initial superposition states of $q_1, |\pm\rangle_x$ and $|\pm\rangle_y$. The background and label colours highlight the parity (purple - odd, orange - even) of the inner qubits and the excitation of each qubit (light - zero, dark - one). Dotted line shows simulation results when taking unwanted ZZ couplings into account. Inset shows the distance from ideal phase as function of number of excitations.

is the measured decay rate of qubit q_n ⁶⁵. The simulation (blue contour plots in Fig. 2) matches well the observed dynamics, suggesting that errors in the transfer are dominated by decoherence. Nonetheless, the excitations partially disperse throughout the chain over time, as can be observed when comparing the qubit populations at times $t = 0, 0.5\tau, \tau, 2\tau$ in subplots (i-iv) to simulation results, shown as black wireframes. While dephasing and flux noise are the main causes of dispersion during the transfer, we attribute this effect also to the hybridisation between qubits q_3 and q_4 .

Equivalent results to the ones shown here are obtained when repeating the same experiment for all initial states and chain lengths varying from three to six qubits (see Supplementary Note 2). However,

notable is the case of the excitation starting on the centre qubit which for odd length chains is the mirror of itself. In this scenario, the excitation fans out into multiple branches and refocuses back at the centre qubit after every transfer time τ .

Parity-dependence of perfect state transfer

The PST protocol produces effective non-local interactions which efficiently transfer single excitations between two distant qubits. However, in the presence of excitations in multiple qubits along the chain, it produces additional interaction terms, therefore effectively coupling all the qubits in the chain. Indeed, the chain Hamiltonian from Eq. (4), shown as grey lines in Fig. 3a, produces stroboscopically equivalent dynamics to the effective non-local parity-dependent Hamiltonian

$$\hat{H}_{\text{PST}}/\hbar = \frac{\pi}{2\tau} \sum_{n=1}^{\lfloor \frac{N}{2} \rfloor} \left(\bigotimes_{k=n+1}^{\hat{n}-1} \hat{\sigma}_k^z \right) (\hat{\sigma}_n^- \hat{\sigma}_{\hat{n}}^+ + \text{h.c.}), \quad (6)$$

shown in Fig. 3a as coloured lines³⁶. Since the dynamics of the two Hamiltonians are equivalent at multiples of the transfer time τ , we can understand the operation generated by the PST protocol through the effective Hamiltonian in Eq. (6). Here, the transversal coupling terms $\sigma^- \sigma^+$ in the sum implement the transfers between the mirror-symmetric qubits at positions n and $\hat{n} = N + 1 - n$. At the same time, the parity operators $\hat{P}_{n+1}^{\hat{n}-1} = \bigotimes_{k=n+1}^{\hat{n}-1} \hat{\sigma}_k^z \in \{-1, 1\}$ modify the sign of the coupling depending on the number parity of excitations between qubits q_n and $q_{\hat{n}}$. Therefore, each mirror-symmetric transfer produces a parity-dependent phase of $\pm \pi/2$, resulting in the effective multi-qubit operation

$$\hat{P} \cdot i\text{SWAP}_n = \begin{bmatrix} 1 & 0 & 0 & 0 \\ 0 & 0 & e^{i\hat{P}_{n+1}^{\hat{n}-1}\pi/2} & 0 \\ 0 & e^{i\hat{P}_{n+1}^{\hat{n}-1}\pi/2} & 0 & 0 \\ 0 & 0 & 0 & 1 \end{bmatrix}. \quad (7)$$

The full PST operation is $U_{\text{PST}} = \bigotimes_{n=1}^{\lfloor \frac{N}{2} \rfloor} \hat{P} \cdot i\text{SWAP}_n$. To intuitively understand the origin of this parity-dependence, we can think of the system of qubits as fermions in a lattice by using a Jordan-Wigner transform^{66,67}. When fermions swap through each other they acquire a phase of π changing the phase of the transferred state from $\pi/2$ to $-\pi/2$ and vice versa. Since the Jordan-Wigner transform leaves the chain Hamiltonian from Eq. (4) unchanged, the fermion and qubit dynamic are equivalent, with the qubit experiencing the same phase changes.

The parity-dependence can be observed explicitly by monitoring the evolution of the superposition state $|+\rangle_x \equiv (|0\rangle_n + |1\rangle_n)/\sqrt{2}$, prepared on qubit q_n . When PST is applied, the state is transferred to $q_{\hat{n}}$ and acquires a phase conditioned on the number of encountered excitations, i.e. $|+\rangle_x \rightarrow |+\rangle_y \equiv (|0\rangle_{\hat{n}} \pm i|1\rangle_{\hat{n}})/\sqrt{2}$, where the sign depends on the number parity. This mechanism is shown on the Bloch sphere in Fig. 3b for a transfer from qubit q_2 to q_5 on a $N=6$ qubit chain.

In our experiment, we verify the parity-dependent property with the transfer between the ends of the chain. We prepare qubit q_1 in a superposition state, apply PST and determine the state of qubit q_6 using quantum state tomography⁶⁸⁻⁷⁰. The density matrix is reconstructed from the tomographic data using a maximum-likelihood estimator while imposing physical constraints⁷¹. The x - y angle of the transferred state is then measured for all possible initial computational states in the inner qubits q_2, q_3, q_4 and q_5 . We repeat the process for four different initial superposition states of $q_1, |\pm\rangle_x$ and $|\pm\rangle_y$, and for each determine the phase acquired during the transfer, as shown in Fig. 3c. As expected, the phase of the transferred state encodes the

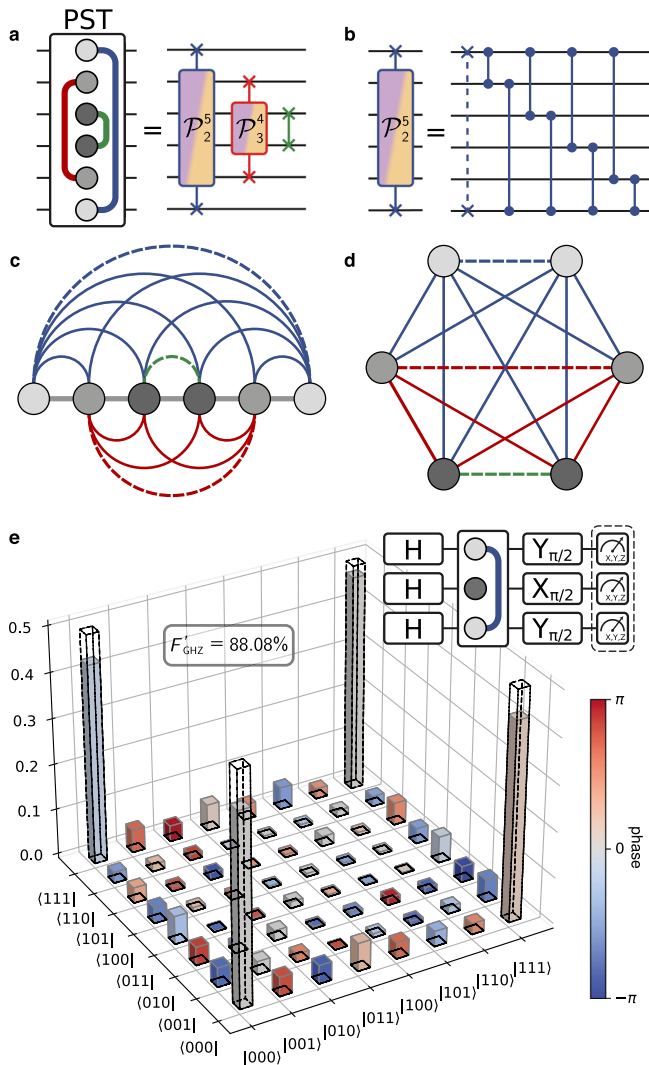


Fig. 4 | Multi-qubit entanglement generation with a single PST operation. Circuit decomposition of the six-qubit PST into iSWAP operations with parity-controlled phases (a) which each decompose further into an iSWAP and multiple CZ gates (b). c Graph representation of the chain with edges corresponding to all effective two-qubit interactions generated by a single PST. Dashed edges denote iSWAP interactions, whereas continuous lines indicate CZ interactions. Colours identify the specific transfer from which each two-qubit interaction originates. d Rearrangement of the chain graph which emphasises the all-to-all connectivity corresponding to a GHZ state. e Reconstructed density matrix of the experimentally realised GHZ state ρ_{exp} (solid bars), with ideal values plotted as black wireframes $\rho_{\text{ideal}} = |\psi_{\text{GHZ}}\rangle\langle\psi_{\text{GHZ}}|$. Allowing for an arbitrary Z rotation of the final state yields $F_{\text{GHZ}} = 88.08\%$. Inset shows the circuit diagram for the GHZ state creation on a chain of size $N = 3$.

parity of the inner qubits, corresponding to $\sim\pi/2$ for an even number of excitations and to $\sim-\pi/2$ when the number parity is odd. We attribute unwanted ZZ interactions to cause deviations from the ideal $\pm\pi/2$ phase. This is supported by the fact that the error in the acquire phase increases linearly with the number of excitation in the inner qubits, as shown in the inset of Fig. 3c. Furthermore, we simulate the PST operation including ZZ interaction with measured strengths ζ_i obtaining good agreement with the observed results [dotted line in Fig. 3c].

Entanglement generation

The parity-dependent property of the PST makes it a powerful tool for generating entanglement between the qubits in a chain. Each of the

effective transfer processes that occurs during PST yields correlations between the state of the transferred qubits and the state of the qubits between them. Therefore, by exploiting the correlations produced by these simultaneous transfers, we can generate entanglement over the whole chain³⁷. This intuition is formalised by using the theory of graph states, a subset of multi-qubit entangled states which are well studied and allow for a simple graphical representation⁷²⁻⁷⁴. In a graph state, nodes represent qubits initialised in the $|+\rangle$ state and edges indicate pairwise Ising $\sigma^z\sigma^z$ (CZ-like) interactions between the nodes. In this formalism, a GHZ state of the form $(|0\dots 0\rangle + |1\dots 1\rangle)/\sqrt{2}$ corresponds up to single-qubit operations to a complete graph, i.e. with all-to-all connectivity. Therefore, a GHZ state can be achieved by preparing the qubits in a superposition state, applying consecutive CZ gates between all pairs of individual qubits and applying a final layer of single qubit gates.

To illustrate how the PST operation maps to the graph state formalism, we decompose it into two-body operations. As derived in Eq. (7) and shown in Fig. 4a for six qubits, the PST can be described by a product of mirror-symmetric transfers, each implementing a parity-dependent iSWAP operation. Each mirror-symmetric transfer can then be decomposed into a single iSWAP gate and a series of CZ gates implementing the parity-dependence, as shown in Fig. 4b. In the graph state representation, each of these two-qubit interactions contributes individual edges between the qubits in the chain, resulting in the all-to-all connected graph shown in Fig. 4c-d. As this remains valid for different qubit numbers, a single PST operation can be utilised to directly generate a GHZ state for any chain length. Note that the iSWAP gates also contribute edges to the graph, since these are equivalent to a CZ gate followed by a SWAP operation and single-qubit Z gates: Given that all qubits are initialised in the $|+\rangle_x$ state, the SWAP operations do not alter the state of the chain, leaving only the Z gates, which commute with the CZ operations and are incorporated in the final layer of single-qubit gates (see Supplementary Note 3).

We demonstrate this process for a chain of three qubits q_5, q_6 and q_1 , using the gate sequence shown in the inset of Fig. 4e, where the PST operation lasts $\tau = 390$ ns. These qubits were chosen to mitigate the adverse impact of residual ZZ interactions, which would affect the PST operation as well as single-qubit gate fidelities. All qubits are prepared in an equal superposition state $|+\rangle_x$ by applying Hadamard gates. Applying a single PST operation entangles the state of the qubits by imparting parity-dependent phases to each of the computational states. Finally, a layer of single-qubit gates maps the fully-entangled graph state onto the GHZ state $|\psi_{\text{GHZ}}\rangle = (|000\rangle + |111\rangle)/\sqrt{2}$. The obtained state ρ_{exp} is determined using quantum state tomography and produces a $F_{\text{GHZ}} = \text{Tr}(\rho_{\text{exp}}^\dagger \rho_{\text{ideal}}) = 84.97\%$ fidelity overlap with the targeted GHZ state, as shown in Fig. 4e. The PST dynamics also result in an additional phase of $e^{i0.378}$ on the $|111\rangle$ state. Since the GHZ state is a superposition of only two computational states, this phase error is equivalent to applying a single-qubit Z rotation. When allowing for this additional phase freedom in the GHZ, we obtain a fidelity of $F'_{\text{GHZ}} = 88.08\%$. The obtained fidelity is close to the simulated decoherence limit of 89.11%.

Discussion

We have experimentally implemented a Perfect State Transfer (PST) protocol on chains of up to six qubits, demonstrating simultaneous control of parametric couplings of multiple neighbouring qubit pairs. This state transfer occurs not only between the qubits at the end of the chain, but also for all mirror-symmetric pairs. Furthermore, in the presence of multiple excitations along the chain, our experiments exhibit parity-dependent properties where the phase of a transferred state depends on the number parity of all excitations within the chain, in good agreement with the theoretical prediction. Harnessing the parity-dependence, we explicitly demonstrate the generation of a GHZ state in a chain of three qubits using a single PST operation with a

fidelity of 88.08%. By mapping the entanglement generation protocol to the theory of graph state, the method can be generalised to larger qubit numbers.

The two main sources of errors in our implementation of PST are decoherence during the gate and residual ZZ couplings. The effect of decoherence in our system can be overcome by increasing the strength of the static capacitive couplings g_{ij} to achieve faster transfers, as well as by increasing the E_J/E_C ratio to suppress dephasing due to charge noise. Precise targeting of qubit frequencies would allow to operate the qubits in the straddling regime ($|\omega_{q_i} - \omega_{q_j}| < \alpha_{q_i/q_j}$) where the ZZ coupling can be fully suppressed^{58,75}. Alternatively, additional drives can be used to control and cancel out these unwanted couplings^{76–79}.

By harnessing simultaneous interactions with no additional all-to-one resources, PST provides an efficient way to implement effective operations between distant qubits on the same or on different chips and create many-qubit entanglement. Compared to its decomposition into single- and two-qubit gates, PST results in a two-fold reduction in total gate time³⁶ and exhibits increased robustness to coherent and incoherent errors (see Supplementary Note 4 for details), presenting a useful tool in the pursuit to create large-scale quantum computers. For example, PST could be used for applications in parity-check codes. Here, the transfer and measurement of a superposition state between the outer qubits in a chain, as implemented in this work, realises a direct parity measurement of the other $N - 2$ qubits. Furthermore, realising PST on overlapping chains opens up the possibility to generate different classes of graph state⁸⁰ and enable quantum routing⁸¹, with potential applications in quantum communication^{82,83} and quantum sensing⁸⁴. Besides purely unitary operations, we note that GHZ states can also be generated in constant depth via measurement-based circuits^{85–90}.

In addition to the discussed applications, the PST protocol can be extended and modified in a number of ways. By introducing detunings between the qubits, the method can be generalised to implement Fractional State Transfer^{36,91–95}, where excitations only partially transfer between mirror-symmetric qubits. The fractional transfer operation exhibits the same parity-dependent property of PST (see experimental results in Supplementary Note 5), which allows for performing small evolution steps of the effective parity-dependent interactions, Eq. (6), enabling simulation of fermionic systems⁹⁶ and gauge field theories⁹⁷. Chain Hamiltonians can also be tailored to implement more general types of transfers, e.g. from one qubit to many, thus allowing for the generation of larger classes of entangled states^{98,99}. Moreover, extending the couplings to allow for time-dependent control provides further speed-ups¹⁰⁰ and enables the exploration of a large family of multi-qubit operations¹⁰¹. Finally, PST can be generalised to operate in networks with higher connectivity: analytical solutions for coupling strengths resulting in PST have been found for hyper-cubes and other cube-like graphs^{102–104}, triangular lattices^{105–107}, multi-layer hexagonal lattices¹⁰⁸, as well as any network which can be described as intersections of one-dimensional chains^{38,109}. The latter results provide a direct implementation in higher-dimensional grid lattices, as shown in Supplementary Note 6.

Methods

Calibration of parametric drives

To control the strength of the simultaneous parametric couplings, we perform multiple rounds of calibration. First, we characterise the effective coupling strengths J_i for each pair of neighbouring qubits as a function of the parametric drive amplitude A_i while all other drives ($A_{j \neq i}$) are set to zero. For each amplitude, we measure the population of the two qubits involved while varying the drive duration and frequency. The resulting Chevron patterns are then fitted to Rabi oscillations in order to estimate the effective coupling strengths $J_i(A_i)$ and

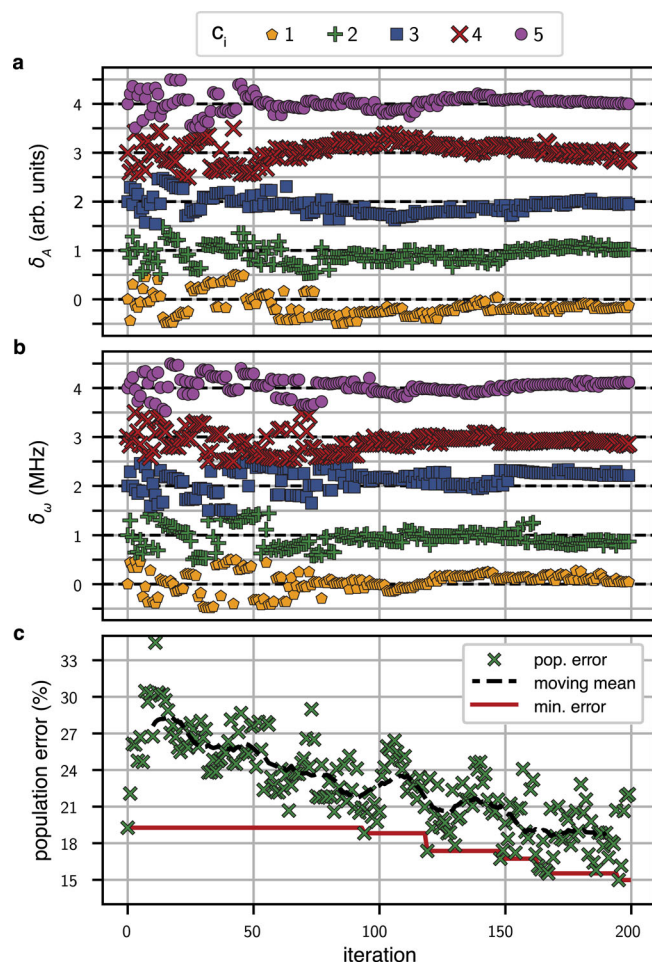


Fig. 5 | Optimisation of simultaneous drives for PST on the six-qubit chain.

Parameter changes as a function of optimiser iteration are shown for drive amplitudes (a) and drive frequencies (b). Results for the five parametric drives are offset for visualisation, with dashed black lines showing their initial value. For reference, the average drive amplitude is 0.21 (arb. units) and the average drive frequency is 183 MHz. c Population errors averaged over all qubits over up to five consecutive transfers. Black dashed line and red line indicate the moving mean and minimum of the error respectively.

the resonant transition frequencies. The obtained values deviate slightly from Eq. (3) due to frequency collisions and higher-order corrections. In particular, the transition frequencies are shifted from the expected qubit-qubit detunings Δ_i due to drive-induced Stark shifts. Given the required PST coupling strengths from Eq. (5), we are then able to set the drive amplitude and frequency accordingly. For each pair, we repeat the same procedure while also driving the two neighbouring couplers off-resonantly. This allows us to correct up to first order the qubit frequency shifts caused by neighbouring simultaneous drives.

As a final step, we apply all drives needed for PST simultaneously and fine-tune all amplitudes and frequencies using an optimiser enabled with experiment feedback. The experiment consists of transferring a single excitation from any initial qubit, with populations in all qubits measured at intervals up to five times the transfer time τ . The resulting average population error, calculated from an ideal transfer, is then fed to a Tree-Structured Parzen Estimator optimiser provided in the Optuna Python library¹¹⁰. Convergence of the closed-loop optimiser is shown in Fig. 5 for transferring an excitation initially prepared on qubit q_1 through a chain of six qubits. Convergence of the closed-loop optimiser results in drive parameters accounting for all cross-

dependencies and thus reducing the transfer error, as shown in Fig. 5 for a chain of $N=6$ qubits.

Data availability

All relevant data supporting the main conclusions and figures of the document are available upon request.

References

- Acharya, R. et al. Suppressing quantum errors by scaling a surface code logical qubit. *Nature* **614**, 676 (2023).
- Kim, Y. et al. Evidence for the utility of quantum computing before fault tolerance. *Nature* **618**, 500 (2023).
- Bluvstein, D. et al. Logical quantum processor based on reconfigurable atom arrays. *Nature* **626**, 58 (2023).
- Feng, L. et al. Continuous symmetry breaking in a trapped-ion spin chain. *Nature* **623**, 713 (2023).
- Iqbal, M. et al. Non-Abelian topological order and anyons on a trapped-ion processor. *Nature* **626**, 505 (2024).
- Mills, A. R. et al. Shuttling a single charge across a one-dimensional array of silicon quantum dots. *Nat. Commun.* **10**, 1063 (2019).
- Yoneda, J. et al. Coherent spin qubit transport in silicon. *Nat. Commun.* **12**, 4114 (2021).
- Pino, J. M. et al. Demonstration of the trapped-ion quantum CCD computer architecture. *Nature* **592**, 209 (2021).
- Bluvstein, D. et al. A quantum processor based on coherent transport of entangled atom arrays. *Nature* **604**, 451 (2022).
- Burton, W. C. et al. Transport of multispecies ion crystals through a junction in a radio-frequency Paul trap. *Phys. Rev. Lett.* **130**, 173202 (2023).
- Künne, M. et al. The SpinBus architecture for scaling spin qubits with electron shuttling. *Nat. Commun.* **15**, 4977 (2024).
- Gu, X. et al. Fast multiqubit gates through simultaneous two-qubit gates. *PRX Quantum* **2**, 040348 (2021).
- Zhang, K. et al. Synthesizing five-body interaction in a superconducting quantum circuit. *Phys. Rev. Lett.* **128**, 190502 (2022).
- Baker, A. J. et al. Single shot i-Toffoli gate in dispersively coupled superconducting qubits. *Appl. Phys. Lett.* **120**, 054002 (2022).
- Kim, Y. et al. High-fidelity three-qubit iToffoli gate for fixed-frequency superconducting qubits. *Nat. Phys.* **18**, 783 (2022).
- Warren, C. W. et al. Extensive characterization and implementation of a family of three-qubit gates at the coherence limit. *npj Quantum Inf.* **9**, 44 (2023).
- Mezzacapo, A., Lamata, L., Filipp, S. & Solano, E. Many-body interactions with tunable-coupling transmon qubits. *Phys. Rev. Lett.* **113**, 050501 (2014).
- Song, C. et al. 10-qubit entanglement and parallel logic operations with a superconducting circuit. *Phys. Rev. Lett.* **119**, 180511 (2017).
- Hazra, S. et al. Ring-resonator-based coupling architecture for enhanced connectivity in a superconducting multiqubit network. *Phys. Rev. Appl.* **16**, 024018 (2021).
- Lu, M. et al. Multipartite entanglement in Rabi-driven superconducting qubits. *PRX Quantum* **3**, 040322 (2022).
- Glaser, N. J., Roy, F. & Filipp, S. Controlled-controlled-phase gates for superconducting qubits mediated by a shared tunable coupler. *Phys. Rev. Appl.* **19**, 044001 (2023).
- Cook, R. J. & Shore, B. W. Coherent dynamics of N -level atoms and molecules. III. An analytically soluble periodic case. *Phys. Rev. A* **20**, 539 (1979).
- Peres, A. Reversible logic and quantum computers. *Phys. Rev. A* **32**, 3266 (1985).
- Christandl, M., Datta, N., Ekert, A. & Landahl, A. J. Perfect state transfer in quantum spin networks. *Phys. Rev. Lett.* **92**, 187902 (2004).
- Nikolopoulos, G. M., Petrosyan, D. & Lambropoulos, P. Electron wavepacket propagation in a chain of coupled quantum dots. *J. Phys.: Condens. Matter* **16**, 4991 (2004).
- Albanese, C., Christandl, M., Datta, N. & Ekert, A. Mirror inversion of quantum states in linear registers. *Phys. Rev. Lett.* **93**, 230502 (2004).
- Yung, M. H., Leung, D. & Bose, S. An exact effective two-qubit gate in a chain of three spins. *Quantum Inform. Comput.* **4**, <https://doi.org/10.26421/QIC4.3-2> (2004).
- Yung, M.-H. & Bose, S. Perfect state transfer, effective gates, and entanglement generation in engineered bosonic and fermionic networks. *Phys. Rev. A* **71**, 032310 (2005).
- Shi, T., Li, Y., Song, Z. & Sun, C.-P. Quantum-state transfer via the ferromagnetic chain in a spatially modulated field. *Phys. Rev. A* **71**, 032309 (2005).
- Karbach, P. & Stolze, J. Spin chains as perfect quantum state mirrors. *Phys. Rev. A* **72**, 030301 (2005).
- Petrosyan, D. & Lambropoulos, P. Coherent population transfer in a chain of tunnel coupled quantum dots. *Opt. Commun.* **264**, 419 (2006).
- Vinet, L. & Zhedanov, A. How to construct spin chains with perfect state transfer. *Phys. Rev. A* **85**, 012323 (2012).
- Vinet, L. & Zhedanov, A. Para-Krawtchouk polynomials on a bi-lattice and a quantum spin chain with perfect state transfer. *J. Phys. A: Math. Theor.* **45**, 265304 (2012).
- Nikolopoulos, G. M. et al. *Quantum state transfer and network engineering*. <https://link.springer.com/book/10.1007/978-3-642-39937-4> (Springer 2014).
- Loft, N. J. S., Marchukov, O. V., Petrosyan, D. & Zinner, N. T. Tunable self-assembled spin chains of strongly interacting cold atoms for demonstration of reliable quantum state transfer. *N. J. Phys.* **18**, 045011 (2016).
- Nägele, M., Schweizer, C., Roy, F. & Filipp, S. Effective nonlocal parity-dependent couplings in qubit chains. *Phys. Rev. Res.* **4**, 033166 (2022).
- Clark, S. R., Alves, C. M. & Jaksch, D. Efficient generation of graph states for quantum computation. *N. J. Phys.* **7**, 124 (2005).
- Kay, A. Perfect, efficient, state transfer and its application as a constructive tool. *Int. J. Quantum Inf.* **8**, 641 (2010).
- Brougham, T., Nikolopoulos, G. & Jex, I. Perfect transfer of multiple excitations in quantum networks. *Phys. Rev. A* **83**, 022323 (2011).
- Mádi, Z., Brutscher, B., Schulte-Herbrüggen, T., Brüscheweiler, R. & Ernst, R. Time-resolved observation of spin waves in a linear chain of nuclear spins. *Chem. Phys. Lett.* **268**, 300 (1997).
- Zhang, J. et al. Simulation of Heisenberg XY interactions and realization of a perfect state transfer in spin chains using liquid nuclear magnetic resonance. *Phys. Rev. A* **72**, 012331 (2005).
- Álvarez, G. A. et al. Perfect state transfers by selective quantum interferences within complex spin networks. *Phys. Rev. A* **81**, 060302 (2010).
- Bellec, M., Nikolopoulos, G. M. & Tzortzakis, S. Faithful communication Hamiltonian in photonic lattices. *Opt. Lett.* **37**, 4504 (2012).
- Perez-Leija, A. et al. Coherent quantum transport in photonic lattices. *Phys. Rev. A* **87**, 012309 (2013).
- Chapman, R. J. et al. Experimental perfect state transfer of an entangled photonic qubit. *Nat. Commun.* **7**, 1 (2016).
- Signoles, A. et al. Coherent transfer between low-angular-momentum and circular Rydberg states. *Phys. Rev. Lett.* **118**, 253603 (2017).
- Li, X. et al. Perfect quantum state transfer in a superconducting qubit chain with parametrically tunable couplings. *Phys. Rev. Appl.* **10**, 054009 (2018).
- Tian, T. et al. Perfect coherent transfer in an on-chip reconfigurable nanoelectromechanical network. *Phys. Rev. B* **101**, 174303 (2020).
- Burkhart, L. D. et al. Error-detected state transfer and entanglement in a superconducting quantum network. *PRX Quantum* **2**, 030321 (2021).

50. Karamlou, A. H. et al. Quantum transport and localization in 1d and 2d tight-binding lattices. *npj Quantum Inf.* **8**, 35 (2022).
51. Zhang, C. et al. Fast and perfect state transfer in superconducting circuit with tunable coupler. *Chin. Phys. B* **32**, 110305 (2023).
52. Xiang, L. et al. Enhanced quantum state transfer by circumventing quantum chaotic behavior. *Nat. Commun.* **15**. <https://doi.org/10.1038/s41467-024-48791-3> (2024).
53. Koch, J. et al. Charge-insensitive qubit design derived from the Cooper pair box. *Phys. Rev. A* **76**, 042319 (2007).
54. McKay, D. C. et al. Universal gate for fixed-frequency qubits via a tunable bus. *Phys. Rev. Appl.* **6**, 064007 (2016).
55. Bravyi, S., Sheldon, S., Kandala, A., McKay, D. C. & Gambetta, J. M. Mitigating measurement errors in multiqubit experiments. *Phys. Rev. A* **103**, 042605 (2021).
56. Roth, M. et al. Analysis of a parametrically driven exchange-type gate and a two-photon excitation gate between superconducting qubits. *Phys. Rev. A* **96**, 062323 (2017).
57. Strauch, F. W. et al. Quantum logic gates for coupled superconducting phase qubits. *Phys. Rev. Lett.* **91**, 167005 (2003).
58. Sung, Y. et al. Realization of high-fidelity CZ and ZZ-Free iSWAP gates with a tunable coupler. *Phys. Rev. X* **11**, 021058 (2021).
59. Huber, G. B. P. et al. Parametric multi-element coupling architecture for coherent and dissipative control of superconducting qubits. <https://arxiv.org/abs/2403.02203> ArXiv 2403.02203 (2024).
60. Petrescu, A. et al. Accurate methods for the analysis of strong-drive effects in parametric gates. *Phys. Rev. Appl.* **19**, 044003 (2023).
61. Yung, M.-H. Quantum speed limit for perfect state transfer in one dimension. *Phys. Rev. A* **74**, 030303 (2006).
62. Kay, A., Xie, W. & Tamon, C. A note on the speed of perfect state transfer. <https://arxiv.org/abs/1609.01854> ArXiv 1609.01854 (2022).
63. Werninghaus, M. et al. Leakage reduction in fast superconducting qubit gates via optimal control. *npj Quantum Inf.* **7**, 1 (2021).
64. Glaser, N. J. et al. Sensitivity-adapted closed-loop optimization for high-fidelity controlled-z gates in superconducting qubits, <https://arxiv.org/abs/2412.17454> ArXiv 2412.17454 (2024).
65. Magnard, P. et al. Fast and unconditional all-microwave reset of a superconducting qubit. *Phys. Rev. Lett.* **121**, 060502 (2018).
66. Jordan, P. & Wigner, E. Über das Paulische Äquivalenzverbot. *Z. f.ür. Phys.* **47**, 631 (1928).
67. Ortiz, G., Gubernatis, J. E., Knill, E. & Laflamme, R. Quantum algorithms for fermionic simulations. *Phys. Rev. A* **64**, 022319 (2001).
68. Chuang, I. L., Gershenfeld, N., Kubinec, M. G. & Leung, D. W. Bulk quantum computation with nuclear magnetic resonance: theory and experiment. *Proc. R. Soc. Lond. Ser. A: Math. Phys. Eng. Sci.* **454**, 447 (1998).
69. Liu, Y.-x., Wei, L. F. & Nori, F. Tomographic measurements on superconducting qubit states. *Phys. Rev. B* **72**, 014547 (2005).
70. Steffen, M. et al. Measurement of the entanglement of two superconducting qubits via state tomography. *Science* **313**, 1423 (2006).
71. Hradil, Z., Řeháček, J., Fiurášek, J., & Ježek, M. *Maximum-Likelihood Methods in Quantum Mechanics, in Quantum State Estimation*, Paris, M. and Řeháček, J. https://doi.org/10.1007/978-3-540-44481-7_3 pp.59–112 (Springer, Berlin, Heidelberg, 2004).
72. Hein, M., Eisert, J. & Briegel, H. J. Multiparty entanglement in graph states. *Phys. Rev. A* **69**, 062311 (2004).
73. Van den Nest, M., Dehaene, J. & De Moor, B. Graphical description of the action of local Clifford transformations on graph states. *Phys. Rev. A* **69**, 022316 (2004).
74. Hein, M. et al. Entanglement in graph states and its applications. *Quantum Computers, Algorithms and Chaos*. 115 <https://doi.org/10.3254/978-1-61499-018-5-115> (2006).
75. Sete, E. A., Chen, A. Q., Manenti, R., Kulshreshtha, S. & Poletto, S. Floating tunable coupler for scalable quantum computing architectures. *Phys. Rev. Appl.* **15**, 064063 (2021).
76. Ni, Z. et al. Scalable method for eliminating residual ZZ interaction between superconducting qubits. *Phys. Rev. Lett.* **129**, 040502 (2022).
77. Ganzhorn, M., Egger, D. J., Filipp, S., Von Salis, G. R. & Moll, N. Cross-talk compensation in quantum processing devices. <https://patents.google.com/patent/US10452991/en> US Patent 10,452,991 (2019).
78. Noguchi, A. et al. Fast parametric two-qubit gates with suppressed residual interaction using the second-order nonlinearity of a cubic transmon. *Phys. Rev. A* **102**, 062408 (2020).
79. Wei, K. X. et al. Hamiltonian engineering with multicolor drives for fast entangling gates and quantum crosstalk cancellation. *Phys. Rev. Lett.* **129**, 060501 (2022).
80. Angelakis, D. G. & Kay, A. Weaving light-matter qubits into a one way quantum computer. *N. J. Phys.* **10**, 023012 (2008).
81. Dutta, S. Quantum routing in planar graph using perfect state transfer. *Quantum Inf. Process.* **22**, 383 (2023).
82. Azuma, K., Tamaki, K. & Lo, H.-K. All-photon quantum repeaters. *Nat. Commun.* **6**, 6787 (2015).
83. Borregaard, J. et al. One-way quantum repeater based on near-deterministic photon-emitter interfaces. *Phys. Rev. X* **10**, 021071 (2020).
84. Shettell, N. & Markham, D. Graph states as a resource for quantum metrology. *Phys. Rev. Lett.* **124**, 110502 (2020).
85. Ristè, D. et al. Deterministic entanglement of superconducting qubits by parity measurement and feedback. *Nature* **502**, 350 (2013).
86. Buhrman, H., Folkertsma, M., Loff, B. & Neumann, N. M. P. State preparation by shallow circuits using feed forward. *Quantum* **8**, 1552 (2024).
87. Foss-Feig, M. et al. Experimental demonstration of the advantage of adaptive quantum circuits, <https://arxiv.org/abs/2302.03029> ArXiv 2302.03029 (2023).
88. Koh, J. M., Koh, D. E., & Thompson, J. Readout error mitigation for mid-circuit measurements and feedforward. <https://arxiv.org/abs/2406.07611> ArXiv 2406.07611 (2024).
89. Alam, F. & Clark, B. K. Learning dynamic quantum circuits for efficient state preparation. <https://arxiv.org/abs/2410.09030> ArXiv 2410.09030 (2024).
90. Bäumer, E. et al. Efficient long-range entanglement using dynamic circuits. *PRX Quantum* **5**, 030339 (2024).
91. Dai, L., Feng, Y. P. & Kwek, L. C. Engineering quantum cloning through maximal entanglement between boundary qubits in an open spin chain. *J. Phys. A: Math. Theor.* **43**, 035302 (2009).
92. Banchi, L., Compagno, E. & Bose, S. Perfect wave-packet splitting and reconstruction in a one-dimensional lattice. *Phys. Rev. A* **91**, 052323 (2015).
93. Genest, V. X., Vinet, L. & Zhedanov, A. Quantum spin chains with fractional revival. *Ann. Phys.* **371**, 348 (2016).
94. Lemay, J.-M., Vinet, L. & Zhedanov, A. An analytic spin chain model with fractional revival. *J. Phys. A: Math. Theor.* **49**, 335302 (2016).
95. Chan, A., Coutinho, G., Tamon, C., Vinet, L. & Zhan, H. Quantum fractional revival on graphs. *Discret. Appl. Math.* **269**, 86 (2019).
96. Arute, F. et al. Observation of separated dynamics of charge and spin in the Fermi-Hubbard model. <https://arxiv.org/abs/2010.07965> ArXiv 2010.07965 (2020).
97. Mildenerger, J., Mruczkiewicz, W., Halimeh, J. C., Jiang, Z. & Hauke, P. Confinement in a \mathbb{Z}_2 lattice gauge theory on a quantum computer. *Nat. Phys.* <https://doi.org/10.1038/s41567-024-02723-6> (2025).
98. Kay, A. Generating quantum states through spin chain dynamics. *N. J. Phys.* **19**, 043019 (2017).
99. Kay, A. Tailoring spin chain dynamics for fractional revivals. *Quantum* **1**, 24 (2017).
100. Caneva, T. et al. Optimal control at the quantum speed limit. *Phys. Rev. Lett.* **103**, 240501 (2009).

101. Nägele, M. Engineering non-local parity-dependent quantum gate in qubit chains master's thesis. Ludwig-Maximilians-Universität München (2022).
102. Christandl, M. et al. Perfect transfer of arbitrary states in quantum spin networks. *Phys. Rev. A* **71**, 032312 (2005).
103. Facer, C., Twamley, J. & Cresser, J. Quantum Cayley networks of the hypercube. *Phys. Rev. A* **77**, 012334 (2008).
104. Bernasconi, A., Godsil, C. & Severini, S. Quantum networks on cubelike graphs. *Phys. Rev. A* **78**, 052320 (2008).
105. Miki, H., Tsujimoto, S., Vinet, L. & Zhedanov, A. Quantum-state transfer in a two-dimensional regular spin lattice of triangular shape. *Phys. Rev. A* **85**, 062306 (2012).
106. Post, S. Quantum perfect state transfer in a 2D lattice. *Acta Appl. Math.* **135**, 209 (2015).
107. Miki, H., Tsujimoto, S. & Vinet, L. Perfect state transfer in two dimensions and the bivariate dual-Hahn polynomials. *Prog. Theor. Exp. Phys.* **2022**, 053A01 (2022).
108. Karimpour, V., Rad, M. S. & Asoudeh, M. Perfect quantum state transfer in two- and three-dimensional structures. *Phys. Rev. A* **85**, 010302 (2012).
109. Pemberton-Ross, P. J. & Kay, A. Perfect quantum routing in regular spin networks. *Phys. Rev. Lett.* **106**, 020503 (2011).
110. Akiba, T., Sano, S., Yanase, T., Ohta, T. & Koyama, M. Optuna: a next-generation hyperparameter optimization framework, in <https://doi.org/10.1145/3292500.3330701> *Proceedings of the 25th ACM SIGKDD International Conference on Knowledge Discovery & Data Mining* (Association for Computing Machinery, 2019) p.2623–2631.

Acknowledgements

We thank Ignacio Cirac, Peter Rabl and Xavier Coiteux-Roy for insightful discussions and helpful comments. This work received financial support by the European Union's Horizon 2020 research, the innovation program 'MOlecular Quantum Simulations' (MOQS; Nr. 955479), the EU MSCA Cofund 'International, interdisciplinary and intersectoral doctoral program in Quantum Science and Technologies' (QUSTEC; Nr. 847471), the BMBF programs 'German Quantum Computer based on Superconducting Qubits' (GeQCoS; Nr. 13N15680) and MUNIQ-SC (Nr. 13N16188), the German Research Foundation project 'Multi-qubit gates for the efficient exploration of Hilbert space with superconducting qubit systems' (Nr. 445948657) and the excellence initiative 'Munich Center for Quantum Science and Technology' (MCQST; Nr. 390814868) as well as the Munich Quantum Valley, which is supported by the Bavarian state government with funds from the Hightech Agenda Bayern Plus. F.P. has received funding from the BMW group and C. Schw. has received funding from LMUexcellent.

Author contributions

F.R. and J.R. designed and carried out the experiments and analysed the data. F.R., J.R. and K.L. performed numerical simulation. I.T. and G.H. designed the chip. L.K., N.B., D.B., L.R. and L.S. fabricated the chip. J.S. designed and procured the cryoperm shields, the PCB and the chip housing. N.G., C.Schw., M.W., M.S., F.P., F.R. and J.R. developed the measurement software framework. F.H., A.M., G.K., C. Schn., F.W., C. Schw., I.T., M.S., L.K., F.R. and J.R. built and maintained the experimental setup. S.F. and M.W. supervised the project.

Competing interests

The authors declare no competing interests.

Additional information

Supplementary information The online version contains supplementary material available at <https://doi.org/10.1038/s41467-025-57818-2>.

Correspondence and requests for materials should be addressed to F. A. Roy or J. H. Romeiro.

Peer review information *Nature Communications* thanks Alexandre Bourassa, Youpeng Zhong, and the other, anonymous, reviewers for their contribution to the peer review of this work. A peer review file is available.

Reprints and permissions information is available at <http://www.nature.com/reprints>

Publisher's note Springer Nature remains neutral with regard to jurisdictional claims in published maps and institutional affiliations.

Open Access This article is licensed under a Creative Commons Attribution 4.0 International License, which permits use, sharing, adaptation, distribution and reproduction in any medium or format, as long as you give appropriate credit to the original author(s) and the source, provide a link to the Creative Commons licence, and indicate if changes were made. The images or other third party material in this article are included in the article's Creative Commons licence, unless indicated otherwise in a credit line to the material. If material is not included in the article's Creative Commons licence and your intended use is not permitted by statutory regulation or exceeds the permitted use, you will need to obtain permission directly from the copyright holder. To view a copy of this licence, visit <http://creativecommons.org/licenses/by/4.0/>.

© The Author(s) 2025